Supplementary Materials for

Oxidation Products of Biogenic Emissions Contribute to Nucleation of Atmospheric Particles

Francesco Riccobono, Siegfried Schobesberger, Catherine E. Scott, Josef Dommen, Ismael K. Ortega, Linda Rondo, João Almeida, Antonio Amorim, Federico Bianchi, Martin Breitenlechner, André David, Andrew Downard, Eimear M. Dunne, Jonathan Duplissy, Sebastian Ehrhart, Richard C. Flagan, Alessandro Franchin, Armin Hansel, Heikki Junninen, Maija Kajos, Helmi Keskinen, Agnieszka Kupc, Andreas Kürten, Alexander N. Kvashin, Ari Laaksonen, Katrianne Lehtipalo, Vladimir Makhmutov, Serge Mathot, Tuomo Nieminen, Antti Onnela, Tuukka Petäjä, Arnaud P. Praplan, Filipe D. Santos, Simon Schallhart, John H. Seinfeld, Mikko Sipilä, Dominick V. Spracklen, Yuri Stozhkov, Frank Stratmann, Antonio Tomé, Georgios Tsagkogeorgas, Petri Vaattovaara, Yrjö Viisanen, Aron Vrtala, Paul E. Wagner, Ernest Weingartner, Heike Wex, Daniela Wimmer, Kenneth S. Carslaw, Joachim Curtius, Neil M. Donahue, Jasper Kirkby, Markku Kulmala, Douglas R. Worsnop, Urs Baltensperger*

*Corresponding author. E-mail: urs.baltensperger@psi.ch

Published 16 May 2014, *Science* **344**, 717 (2014)
DOI: 10.1126/science.1243527

This PDF file includes:

Other Supplementary Material for this manuscript includes the following:
available at www.sciencemag.org/content344/6185/717/suppl/DC1

Supporting Online Material for:

Oxidation Products of Biogenic Emissions Contribute to Nucleation of Atmospheric Particles

by Francesco Riccobono et al.

Materials and Methods

In the CLOUD (Cosmics Leaving OUtdoor Droplets) chamber the sulfuric acid concentration is precisely controlled via OH oxidation of SO_2, while BioOxOrg is produced via OH oxidation of pinanediol (PD, $C_{10}H_{18}O_2$). PD is a model compound for monoterpene oxidation products, which have recently been proposed as key mediators of new-particle formation (*41*) via terpene secondary organic aerosol (*42*). Pinanediol is added to the chamber by flushing clean air through an evaporator containing PD (Sigma Aldrich, 99%) at 69°C, just above its melting point. OH is generated by ozone photolysis driven by uniform UV illumination from a fiber-optic system. All experiments were performed at 278 (±0.01) K and 38% (±2%) relative humidity.

Extreme care was applied to minimize possible contamination to the highest possible extent. After a full cleaning cycle the chamber (including flushing the chamber with water and baking it at 100°C), the contamination by NH_3 and dimethylamine was <2 and <0.1 pptv, respectively. Organic contamination was present, however on a very low level: Schnitzhofer et al. (2013) reported that the total volatile organic compound (VOC) contamination was usually below 1 ppbv (*43*). On average more than 80% of the total VOCs was coming from only 5 exact masses (tentatively assigned as formaldehyde, acetaldehyde, acetone, formic acid, and acetic acid), which have a rather high vapor pressure and are therefore not important for nucleation and growth of particles. Some

additional contamination by dimethylamine was present in these experiments, due to intentional injection of this compound in experiments immediately preceding those described here. This contamination is described in detail below, and it is shown that it is negligible for the determination of the nucleation rates described here.

The gas and the particle phases were monitored by an SO_2 monitor (Enhanced Trace Level SO_2 Analyzer, Model 43i-TLE, Thermo Scientific, USA), an O_3 monitor (TEI 49C, Thermo Environmental Instruments, USA), a dew point mirror hygrometer (DewMaster Chilled Mirror Hygrometer, EdgeTech, USA), a chemical ionization mass spectrometer (CIMS) to measure H_2SO_4 concentration (*44*), a proton transfer reaction time of flight (PTR-TOF) mass spectrometer to measure organic vapor concentrations such as [PD] (*45*), an ion chromatograph (IC) to measure ammonia (NH_3) and dimethylamine (DMA, C_2H_7N) (*46*), two atmospheric pressure interface time of flight (APi-TOF) mass spectrometers to measure the composition of positively and negatively charged clusters (*47*), and a wide array of condensation particle counters (CPC), including a particle size magnifier (PSM; Airmodus 09) (*48*) which was operated in a scanning mode to measure the growth rate of particles smaller than 2.5 nm, two diethylene glycol (DEG) CPCs (*49)*, and a butanol CPC (TSI 3776).

$J_{1.7}$ data were calculated on the one hand directly from the PSM data and on the other hand from the formation rate (dN_2/dt) measured by the DEG CPC with a 50% efficiency (D_{50}) at 2 nm (*50*). In the latter case, the nucleation rates at 2 nm (J_2) are calculated from correcting dN_2/dt for loss of particles due to chamber walls, dilution and coagulation, and $J_{1.7}$ values were then determined at 1.7 nm mobility diameter after correcting J_2 for losses

between 1.7 nm and 2 nm (*51*). However, as the PSM data was not available for all of the runs, and because of its lower time resolution (in scan mode), in order to maximize the data base, the nucleation rates $J_{1.7}$ reported in Fig. 1 are those calculated from the DEG CPC. There is good agreement between the $J_{1.7}$ values determined with these two methods for those cases where PSM data were available, as shown in Fig. S1.

The error on $J_{1.7}$ has three components that are added together in quadrature to estimate the total error indicated in Figs. 1A, 1B and 1C: i) statistical measurement error derived from the scatter of the DEG CPC measurement, evaluated separately for each nucleation event; ii) a ±30% systematic uncertainty on J_2 estimated from the run-to-run reproducibility of dN_2/dt under nominally identical chamber conditions; iii) an estimated +50%/-33% uncertainty on the calculated correction factor $J_{1.7}/J_2$. The error bars in Fig. 1D include only statistical errors since systematic errors largely cancel in calculating the ratio $(J_{\pi/gcr} - J_n) / J_{\pi/gcr}$.

The overall experimental uncertainty on $[H_2SO_4]$ measured by the CIMS is estimated to be +100%/-50%. However, the error bars on sulfuric acid reported in Fig. 1B reflect only the run-to-run relative experimental uncertainty on $[H_2SO_4]$ which is typically ±10%.

In order to disentangle the roles of H_2SO_4 and BioOxOrg on the nucleation rates we designed two sets of experiments varying only $[H_2SO_4]$ or [BioOxOrg] at a time, with each other held nearly constant. During the first set of experiments we measured the nucleation rates at variable concentrations of BioOxOrg (10^6 - $2 \cdot 10^8$ cm^{-3}) by increasing the concentration of PD and maintaining the sulfuric acid concentration in a limited range ($1.9 \pm 0.7 \cdot 10^6$ cm^{-3}), while for the second set of experiments we varied the concentration of H_2SO_4 ($1.6 \cdot 10^6$ - $1.5 \cdot 10^7$ cm^{-3}) by increasing the concentration of SO_2 maintaining the

concentration of BioOxOrg in a limited range ($1.0\pm0.7\cdot10^{8}$ cm^{-3}). These two main sets of experiments were focused to determine the nucleation rates under the three different ionization rates described in the main text, through the sequence "neutral" → "gcr" → "pion beam". The nucleation rates plotted in Figs. 1B, 1C and 1D, and the least-squares fit of Eq. 2 are based only on these two main sets of experiments. We also performed experiments aimed to retrieve additional APi-TOF mass defect plots at only GCR or pion beam conditions, and at [H_2SO_4] and [BioOxOrg] outside of the range of concentrations explored during the two main sets of experiments. As a reference for the APi-TOF mass defect plots shown in Figs. 2, S2, S3, S4, the nucleation rates of these additional experiments are plotted as bold diamonds in Fig. 1A.

Measurements of ion mass spectra using APi-TOF mass spectrometers

APi-TOF mass spectrometers were used during the particle formation experiments at the CLOUD chamber (*32, 47*). The APi-TOF measures the mass-to-charge ratio of ions and ionic clusters of either positive or negative polarity. No ionization of the sample was performed, so only ions charged previously in the CLOUD chamber were detected. The sample was taken from the chamber at atmospheric pressure and entered the instrument via a critical orifice. In the APi-TOF, the ions are accelerated by an electric field and separated by their time-of-flight, which depends on their mass-to-charge ratio, until they are counted on a multi-channel plate detector (MCP). The instrument was adjusted for a detectable range from about 50 to 3300 Thomson (Th) and maximum transmission efficiency from the instrument's inlet to the MCP of 2.3% at 1100 to 1400 Th. Only singly charged ions were detected, therefore the mass-to-charge ratio is identical in value

to the ion's mass expressed in unified atomic mass units (u) or dalton (Da). E.g., 3300 Da correspond to 2.3 nm of mobility-equivalent diameter, when a density of 1300 kg m^{-3} is assumed (*31*).

The composition of ions and ionic clusters is determined primarily from their accurate mass, which is different from the integer ("nominal") mass. The difference is called the mass defect. The nominal mass of an ion is defined as 1/12 of the mass of a ^{12}C atom times the total number of the ion's protons and neutrons. The mass defect is due to the nuclear binding energy of each of the ion's atoms, which is different for different elements. Therefore, an ion of a certain elemental composition has a unique mass defect and accurate mass, which is measured by the APi-TOF at an accuracy of < 10 ppm and a resolving power of 5300 Th/Th. Note that only the elemental composition of an ion can be determined directly (e.g. $H_3S_2O_8^-$). The configuration of the atoms has to be inferred (e.g., $H_2SO_4 \bullet HSO_4^-$).

As an ion's composition defines its mass defect, it is useful to present ion mass spectra as so-called mass defect diagrams (e.g., Fig. 2A). In these diagrams, the mass defect of the ions is plotted against their accurate mass. An ion is shown as a circle at the position corresponding to its composition. The circle size is scaled by the ion $(\text{count rate})^{1/2}$. The addition of a molecule to an ion or ion cluster corresponds to a displacement by a vector unique for that molecule's composition. Therefore, mass defect diagrams result in patterns that are specific to the mechanisms by which such ion clusters grow.

For this study we performed particle formation experiments in the CLOUD chamber following the oxidation of PD to oxidized organic compounds ($C_xH_yO_z$, BioOxOrg) and SO_2 to H_2SO_4. During most of these particle formation experiments, most of the APi-TOF data from negatively charged ions arrange in four broad bands, about 220 Th apart from each other (e.g., Fig. 2A). The transition to each band represents the addition of a BioOxOrg molecule containing 10 carbon atoms. The ions in each band are mainly ion clusters containing such BioOxOrg, plus up to three H_2SO_4 molecules, and a bisulfate ion (HSO_4^-), i.e. $(C_{10}H_xO_y)_m \bullet (H_2SO_4)_{0–3} \bullet HSO_4^-$, where *m* corresponds to the band number. These ion clusters are shown as yellow and orange circles in the mass defect diagrams here (Figs. 2A, S2A, S2B, S3, S4). Each band spans from the upper left to the lower right due to different numbers of oxygen and sulfur atoms involved, because both these elements have negative mass defects. It can be seen from this pattern that a wide range of BioOxOrg are involved in growing these clusters, together with a number of H_2SO_4 molecules, which increases as the clusters grow (e.g., Fig. 2A). The involved BioOxOrg feature a wide range of average carbon oxidation states ($\overline{OS_C}$), and some of them are very highly oxidized ($\overline{OS_C} \geq 0$). A detailed discussion of the chemistry of the observed BioOxOrg is found in (*32*).

This four-band structure appears at the commonly used sulfuric acid concentrations [H_2SO_4] (10^6 to 10^7 cm^{-3}), whenever the concentration of oxidized organics [BioOxOrg] is sufficiently high (~ $2 \cdot 10^7$ cm^{-3}). The latter condition requires a sufficiently high concentration of pinanediol [PD] (> 300 pptv). An increase of [BioOxOrg] is apparent immediately when the UV lights are turned on. This increase is manifest in an increase of signal for bands 2 and larger (Fig. S2). The time from turning on full UV illumination to

the establishment of a new steady-state ion cluster distribution is about one hour. The time series during such transitions also show that the signals of the larger ion clusters appear later than those of the smaller ion clusters, indicative of growth that is driven mainly by the step-wise addition of C_{10}-containing BioOxOrg (Figs. S2C and S2D). The build-up of these larger ion clusters precedes the appearance of still larger particles (>2 nm) counted by CPCs, as expected for the formation of growing new particles (Fig. S2D). Within a few minutes, a DEG CPC (*50*) with a cut-off mobility diameter of 2 nm detects newly formed 2-nm particles. A butanol-based CPC (TSI 3776) with a cut-off at 3 nm then follows within a few more minutes (see also Fig. 2B).

Note that a direct quantitative determination of [BioOxOrg] is not possible using the APi-TOF measurements, because the count rate for each detected ion is dependent on a number of insufficiently understood processes. In particular the efficiencies of transferring electric charge (usually in the form of a proton) between any two molecules or molecular clusters are not quantitatively known.

An interesting feature apparent in the mass defect diagrams is the observation of ion signals located between and beyond the four bands (Figs. 2A, S2B, S3A). Such signal is most pronounced after the second band, visually "connecting" the second and third, and the third and the fourth bands. Similarly, ions are seen growing beyond the fourth band as well. These are likely due to smaller organic compounds (#C < 10) co-condensing onto ion clusters from the second band (mostly $C_{20}H_xO_y \bullet (H_2SO_4)_{0–1} \bullet HSO_4^-$) onwards. Their mass defect locates these clusters close to the lower-right part of the bands, suggesting that either their $\overline{OS_C}$ or their H_2SO_4 content is relatively high. Note that for

small signal levels it is not feasible to unambiguously identify the elemental composition of every ion, especially for the complex patterns for *m/z* > 500.

Figure S3 presents a summary of the ion spectra measured by the APi-TOF during particle formation, as experimental conditions were varied over a wide range of H_2SO_4 and BioOxOrg in the chamber. Under conditions of [H_2SO_4] = 1.8–2.3·10^6 cm^{-3} and calculated [BioOxOrg] = 0.5–1.2 10^8 cm^{-3}, particle formation rates in the chamber were similar to atmospheric observations, as described in the main text (Fig. 1); where the APi-TOF ion spectra consisted mainly of up to the four bands containing one to four C_{10} compounds, as described above (e.g., Figs. S2B, S3A).

When reducing [BioOxOrg], the bands become sequentially weaker in intensity starting from the fourth band, eventually disappearing altogether. E.g., at [BioOxOrg] = 1.1·10^6 cm^{-3}, where no fourth or third band was observed, with very little signal in the second band, and less intensity in the first band as well (Fig. S3D) the measured particle formation rate was much lower. For [BioOxOrg] < 10^7 cm^{-3}, appreciable particle formation rates were only obtained when [H_2SO_4] was increased. The resulting dependency of formation rates on [H_2SO_4] falls outside of the range of atmospheric observations (cf. Fig. 1A). The APi-TOF spectra during these experiments show that larger ion clusters contained small nitrogen-containing bases, mostly NH_3, and H_2SO_4 (Fig. S3C), similar to the clusters observed during CLOUD chamber experiments, which investigated particle formation without organics (*16*). Note that these clusters are only observable at sufficiently high particle formation rates, i.e., in this case at sufficiently high [H_2SO_4] (cf. Figs. S3C, D). Also note that most of these base-acid clusters also

contain one or two dimethylamine (C_2H_7N) molecules. These molecules were present because dimethylamine had been added into the chamber for experiments preceding the experiments reported on here (see *24*), whereas after a full cleaning cycle no dimethylamine was found in the chamber.

As reported in this study, measured particle formation rates were also greatly affected by [H_2SO_4]. Experiments were performed with [H_2SO_4] up to 1.6 10^7 cm^{-3}. When [H_2SO_4] was increased, more H_2SO_4 molecules were present in the ion clusters. The overall intensities of the BioOxOrg bands were suppressed, particularly for higher bands. When increasing [H_2SO_4] beyond 10^7 cm^{-3}, the fourth band started to dissolve and give way to ion signals that appeared less well organized in the mass defect diagram and featured a decreased average mass defect. This trend continued with increasing [H_2SO_4]; at [H_2SO_4] = $1.6 \cdot 10^7$ cm^{-3} the fourth band was essentially gone, while the third band started to dissolve, and the relative signal from the second band decreased as well (Fig. S3B). The ion signals that replaced the fourth band and most of the third band had mostly similar masses, but on average a reduced mass defect. This observation is likely due to smaller organics being able to join the clusters more readily under these conditions, whereas they are less able to do so at lower [H_2SO_4], leading to the dominance of C_{10}-BioOxOrg and the subsequent four-band structure of the mass spectra for those conditions, as presented above.

A closely related trend with increasing [H_2SO_4] is the gradual appearance of clusters of H_2SO_4 with small bases, mainly NH_3. These are the same clusters discussed above for the case of high [H_2SO_4] but low [BioOxOrg], containing mostly also one or two C_2H_7N. Both NH_3 and C_2H_7N were present as contaminants and below the limits of detection by

the ion chromatography measurements from the CLOUD chamber, i.e., [NH_3] < 2 pptv = $5.3 \cdot 10^7$ cm^{-3}, and [C_2H_7N] < 1 pptv = $2.6 \cdot 10^7$ cm^{-3}. These results show that at sufficiently high [H_2SO_4], a non-negligible fraction of H_2SO_4 forms anion clusters with only H_2SO_4, NH_3 and amines even when [BioOxOrg] is comparable to or slightly higher than [NH_3] and [C_2H_7N]. The dependence of these clusters on high [H_2SO_4] likely reflects higher concentrations of H_2SO_4 trimers and tetramers ($(H_2SO_4)_n \bullet HSO_4^-$, n = 2 and 3) under these conditions, because $n \geq 3$ is required to form clusters with NH_3, and $n \geq 2$ is required to form clusters with dimethyl amine, whereas $n \geq 0$ is sufficient to form clusters with large (C≈10) BioOxOrg. Though the composition for most peaks at higher masses (> 700 Da) could not be determined for the cases of relatively high [H_2SO_4], the observed diversity of these ions highly suggests that they include BioOxOrg. Their position in the mass defect diagram further suggests that they contain 10 carbon atoms and more, and very likely many of them H_2SO_4 molecules as well. It is also plausible that at least some of these ions additionally include NH_3 or C_2H_7N. Indeed, such mixed clusters have been identified for these experiments, albeit lighter than 700 Th. The strongest signal among those is usually obtained for $C_{10}H_{16}O_3 \bullet C_2H_7N \bullet (H_2SO_4)_2 \bullet HSO_4^-$, where $C_{10}H_{16}O_3$ may be pinonic acid. It should be noted that the NH_3 and amine contamination levels were similar for all the experiments in Fig. S3, so that the appearance of NH_3 and amine containing clusters reflects the relative strengths of the cluster bonds as [H_2SO_4] and [BioOxOrg] are varied.

Finally, [H_2SO_4] was also reduced to as low concentrations as was possible during our experiments ($5.3 \cdot 10^5$ cm^{-3}). Under these conditions, particle formation rates were practically zero, and H_2SO_4 molecules almost disappeared from the ion clusters detected

by the APi-TOF (Fig. S4). BioOxOrg bands could still be clearly discerned in the corresponding mass defect diagram, similar to those obtained under standard conditions (i.e. with higher [H_2SO_4]), and again the ions in these bands consisted mainly of C_{m*10}-containing BioOxOrg (*m* = band number). However, most BioOxOrg was now observed in clusters with the nitrate ion (NO_3^-) instead of HSO_4^-. This observation is an additional strong indication of the important role of H_2SO_4 clusters with BioOxOrg derived from PD for new-particle formation and growth to larger particles (>2 nm) detectable by particle counters. Note that many of those $C_xH_yO_z \bullet NO_3^-$ clusters were observed under conditions of higher [H_2SO_4], but the spectra were then always dominated by clusters including HSO_4^- (e.g., Figs. 2A, S3A).

Derivation of [BioOxOrg]

PD was chosen as a model compound for first generation oxidation products of monoterpenes. It still has the monoterpene structure but does not react with ozone, consequently it is further oxidized to BioOxOrg only by OH radical reactions. Thus, the concentration of BioOxOrg can be calculated from the PD concentration (measured by the PTR-TOF) and the estimated concentration of OH assuming steady state conditions (where production and loss rates are equal)

$$[\text{BioOxOrg}] = k_{PD,OH}[PD][OH] / (k_{wall} + k_{cond} + k_{dil}) \quad \text{Eq. S1}$$

where the losses (the denominator in the right-hand term part of the equation) include the wall loss rate (k_{wall}), the condensation loss rate (k_{cond}) and the dilution loss rate (k_{dil}) (see below for the derivation of the loss rates). $k_{PD,OH}$ (=$3.9 \cdot 10^{-11}$ cm^3 s^{-1}) is the reaction rate constant between PD and OH. Analogously the concentration of OH was estimated from the measured steady state sulfuric acid concentration.

$$[OH] = [H_2SO_4] (k_{wall}+k_{cond}+k_{dil}) / (k_{SO2,OH}[SO_2]) \quad \text{Eq. S2}$$

The impurities in PD (~1%) produced some artifact H_2SO_4 upon injection. We assume that some of these impurities were alkenes, which underwent ozonolysis and produced H_2SO_4 via the Criegee intermediate (*52*). This background H_2SO_4 (30 to 70%) was subtracted from the measured H_2SO_4 signal when calculating [OH]. A fraction of this background H_2SO_4 could also be due to OH produced by alkene ozonolysis. Assuming that 50% is produced by OH from alkene ozonolysis the concentration of BioOxOrg could therefore be a factor of ~2 higher if the correction due to Criegee radicals only represents an over-correction. Moreover, under GCR and pion beam conditions the CIMS measured a higher sulphuric acid concentration than under neutral conditions. It was found that this apparent increase of H_2SO_4 is not real but an instrumental effect which has been corrected for (see Rondo et al., manuscript submitted to Atmos. Meas. Tech.)

The losses of BioOxOrg are due to wall losses, condensation onto aerosol particles and losses due to replacement of the sampled air of the chamber with clean air (dilution). The wall loss rate is the largest of the three loss terms, at least for experiments run without a

large preexisting aerosol population. The dilution term is the smallest of the three at the used dilution flow of 130 l/min.

For any vapor compound in the CLOUD chamber, the wall loss rate can be calculated as

$$k_{wall}=C_{wall}\,(D_v)^{1/2} \qquad \text{Eq. S3}$$

where D_v is the diffusion coefficient of the vapor and C_{wall} is a pre-factor independent of the specific vapor if one assumes that there is no re-evaporation from the walls. C_{wall} is empirically determined measuring the wall loss rate of sulfuric acid (CIMS) and using the sulfuric acid diffusion coefficient (0.08 cm^2s^{-1}) (*53*).

The error bars of [BioOxOrg] reported in Fig. 1C of the main text are derived from the sum in quadrature of the statistical errors on the measured concentrations at the right-hand side of Eqs. S1 and S2 ([PD], [H_2SO_4] and [SO_2]). The main source of uncertainty in the concentration of BioOxOrg (not shown in Fig. 1C) derives from the error in the choice of the diffusion coefficient of BioOxOrg, the assumption made on the re-evaporation from the walls and from the fact that the calculated OH may be underestimated if the background correction of [H_2SO_4] due to SO_2 oxidation by Criegee radicals is overestimated (see above). The BioOxOrg concentrations shown in Fig. 1C are calculated assuming the same diffusion coefficient and the same C_{wall} (without re-evaporation from the wall) as sulfuric acid which is an upper limit for the $k_{wall,BioOxOrg}$. A sensitivity study shows that if we assume a $k_{wall,BioOxOrg}$ 10 or 100 times smaller than $k_{wall,H2SO4}$, we obtain a factor of ~5 or ~10 higher BioOxOrg concentrations. Decreasing further $k_{wall,BioOxOrg}$ does not increase [BioOxOrg] any further since the wall loss term is

no longer dominant. The variation of [BioOxOrg] due to different $k_{wall,BioOxOrg}$ applies linearly to all the estimated [BioOxOrg], therefore it would affect only the kinetic factor k_m of Equation 2 in the main text but not the exponent q.

Quantum chemical calculations

We used the multi-step method developed by Ortega et al. (*54*) to calculate Gibbs free energies at 278K of clusters of sulfuric acid and 3-methyl-1,2,3-butane-tricarboxylic acid (MBTCA), an oxidation product of α-pinene as well as of PD. The structure of MBTCA is as follows:

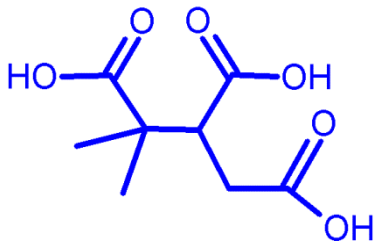

It was chosen because it is one of the few well known compounds formed in such oxidation processes that have a high O:C ratio. The method consists in a geometry optimization and frequency calculation performed with the Gaussian09 program (*55*) using the B3LYP hybrid functional (*56*) and the CBSB7 basis set (*57*), and a single-point electronic energy calculated with the TURBOMOLE program (*58*) using the RI-CC2 method (*59*) and aug-cc-pV(T+d)Z basis set (*60*). We calculated the Gibbs free formation energy of neutral and negatively charged clusters formed with up to two sulfuric acid molecules and up to two organic acids. Gibbs free formation energies for all studied clusters are given in Table S1.

Quantum chemical data for the full set of hydrated clusters is not available at present. The addition of water molecules to the cluster increases the computational effort in different ways. The size of the system increases, resulting in an extension of the computational resources needed for the calculations. Additionally, the number of possible conformers increases combinatorially so the conformational sampling becomes unaffordable. Also, as the degree of water-water bonding grows, the harmonic oscillator and rigid rotor approximation used to estimate Gibbs free energies become less reliable. The presence of water might affect the evaporation rates of the clusters. Almeida et al. (2013) (*24*) showed how in the case of strongly interacting molecules such as dimethylamine (DMA) and sulfuric acid the effect of hydration in the formation rates calculated based on evaporation rates of the clusters was rather small. In the case of MBTCA, the formation free energy of the heterodimer (H_2SO_4 · MBTCA) is close to the formation free energy of H_2SO_4 · DMA, so we expect the effect of hydration in the case of MBTCA to be rather small as well. Nevertheless, the absence of water in the quantum chemical calculations presented here has to be kept in mind when comparing these results with the experimental observations.

We used the calculated Gibbs free formation energies to estimate the evaporation rate of different clusters. Evaporation rates for the neutral and negatively charged clusters studied are shown in Figures S5 and S6, respectively. In the case of neutral clusters, H_2SO_4 · MBTCA clusters are more stable than the corresponding pure sulfuric acid clusters (Fig. S5). For example the evaporation rate of the heterodimer H_2SO_4 · MBTCA is four orders of magnitude smaller than the evaporation rate of the sulfuric acid dimer. The addition of a second molecule of MBTCA to the heterodimer is more favorable than

the addition of a second sulfuric acid molecule. The evaporation rate of the $(H_2SO_4)_2 \cdot (MBTCA)_2$ cluster is more than five orders of magnitude smaller than the evaporation rate of the sulfuric acid pure tetramer. Based on the formation free energies of different clusters, the formation of $(H_2SO_4)_2 \cdot (MBTCA)_2$ by collision of two $H_2SO_4 \cdot MBTCA$ clusters might be an important pathway. However, the most relevant pathway will depend on the relative concentrations of MBTCA, H_2SO_4 and $H_2SO_4 \cdot MBTCA$ clusters.

In the case of negatively charged $H_2SO_4 \cdot MBTCA$ clusters, the (1,1) cluster is slightly less stable than the pure sulfuric acid dimer (Fig. S6). But despite this difference, the evaporation rate of the negatively charged heterodimer is so low that, as in the case of the pure sulfuric acid charged dimer, it is negligible. The evaporation rate of the (2,1) cluster is around two orders of magnitude larger than the evaporation rate of the pure sulfuric trimer, but again is relatively small. In contrast to neutral clusters, in the case of negatively charged clusters, the addition of a second sulfuric acid molecule to the heterodimer is more favorable than the addition of a second MBTCA molecule. The evaporation rate of the $HSO_4^- \cdot H_2SO_4 \cdot (MBTCA)_2$ cluster is around two orders of magnitude smaller than of the pure sulfuric acid charged tetramer $HSO_4^- \cdot (H_2SO_4)_3$.

Another caveat is that MBTCA has an O:C ratio of 0.75 while many molecules with an O:C ratio of up to 1 were found; recently, a mechanism for rapid formation of such highly oxidized molecules was reported (*61*,*62*). As the evaporation rates of the clusters typically decrease with increasing O:C it is expected that some clusters do exist that are substantially more stable than the MBTCA results suggest. Additionally, a very wide range of oxidized organic compounds were found clustered with sulfuric acid, as revealed by the APi-TOF measurements (details in (*32*)). $C_8H_{12}O_6$ (conceivably MBTCA) was but

one of these observed compounds. In the pursuit of a more complete understanding of the details of plausible clustering mechanisms, future quantum-chemical calculations will have to explore many more monoterpene oxidation products still.

Global Atmospheric Modelling

The GLObal Model of Aerosol Processes (GLOMAP) was used to assess the impact of this new parameterization for atmospheric nucleation. GLOMAP is an extension to the TOMCAT chemical transport model (*63*) and has previously been described extensively (*11, 35*). GLOMAP operates at a horizontal resolution of 2.8^{o} x 2.8^{o} with 31 σ-pressure levels extending to 10 hPa. Here we use GLOMAP-mode (version 6), in which information about aerosol component masses and number concentrations is carried in five log-normal size modes; four hydrophilic (nucleation, Aitken, accumulation and coarse), and a non-hydrophilic Aitken mode. Material in the particle phase is classified into four components: sulfate, black carbon, particulate organic matter, and sea-salt. GLOMAP includes representations of nucleation, particle growth via coagulation, condensation and cloud processing, wet and dry deposition and in/below cloud scavenging. Model simulations are performed for the year 2000, with 3 months spin-up from zero initial aerosol. Meteorology is taken from European Centre for Medium-Range Weather Forecasts (ECMWF) reanalyses at 6-hourly intervals and cloud fields from the International Satellite Cloud Climatology Project (ISCCP) archive (http://isccp.giss.nasa.gov/). Lumped monoterpene emissions are taken from the Global Emissions InitiAtive (GEIA) database (*36)* giving a total annual emission of 127 TgC. In

GLOMAP monoterpenes are oxidized by NO_3, O_3 and OH, (assuming the reaction characteristics of α-pinene) to form a secondary organic material that condenses irreversibly onto existing aerosol.

We performed four simulations to examine the impact of different nucleation mechanisms on total particle concentrations. Each model run is identical in every other respect (i.e., they have the same primary aerosol and precursor gas emissions):

A) Binary homogenous nucleation (BHN) of H_2SO_4 and H_2O only (*64*)

B) BHN plus activation boundary layer nucleation (BHN + $k_{ACT}[H_2SO_4]$) parameterized according to Eq. 1 with $k_{ACT} = 2 \cdot 10^{-6}$ s^{-1} (*64*)

C) BHN plus $k_{MET}[H_2SO_4][NucOrg]$ with $k_{MET} = 5 \cdot 10^{-13}$ s^{-1} (*25*) .

D) BHN plus Eq. 2 (BHN + $k_m[H_2SO_4]^2[BioOxOrg]$) throughout the atmosphere with $k_m = 3.27 \cdot 10^{-21}$ cm^6 s^{-1}.

For simulation D, the atmospheric concentration of BioOxOrg is calculated according to Eq. S1, assuming that:

$$d[PD]/dt = k_{\alpha\text{-pin,OH}}[\alpha\text{-pin}][OH] - k_{PD,OH}[PD][OH] \quad \text{Eq. S4}$$

and therefore, at steady state:

$$[PD] = (k_{\alpha\text{-pin,OH}}[\alpha\text{-pin}]) / k_{PD,OH} \quad \text{Eq. S5}$$

where $k_{\alpha\text{-pin,OH}} = 1.2 \cdot 10^{-11} \exp(444/T)$ (*65*). Loss of BioOxOrg to the chamber walls (rate k_{wall}) is assumed to be the dominant loss term in Eq. S1. In the global model, k_{wall} is replaced with k_{CS}, the atmospheric condensation sink (i.e. rate of condensation onto existing particles, s^{-1}), calculated assuming the diffusion characteristics of a typical α-pinene oxidation product (see Appendix A1 of (*66*)). The simulated nucleation rate at 1.7 nm diameter (i.e. Eq. 2) then becomes:

$$J_{1.7} = k_m [H_2SO_4]^2 [(k_{\alpha\text{-pin,OH}}[\alpha\text{-pin}][OH])/k_{CS}] \quad \text{Eq. S6}$$

where [α-pin] is the concentration of our lumped monoterpene tracer in the model.

Figure S7 shows simulated monthly mean particle number concentrations (greater than 3 nm diameter) in January and June for simulation D (BHN + $k_m[H_2SO_4]^2$[BioOxOrg]).

Multi-annual observations of total particle number concentration were obtained from a previously compiled dataset (*11*). Here we use data collected at 19 out of the 20 continental boundary layer locations, listed in Table S2; data from Botsalano, South Africa, are excluded in order to sample from northern hemisphere land locations with the same seasonality. The definition of the particle number concentration varies between sites depending on the type of instrument used (they vary from N>3nm to N>14 nm; see (*11*) and Table S2). The same definition was used when sampling from the model. Model data were interpolated to the observation location in the horizontal, and in the vertical where necessary.

Figure S8 shows the correlation between the modelled and observed particle concentrations for each month. We also calculated the Pearson correlation coefficient (R) between measured and simulated monthly mean particle concentrations at each location across the 12 months; the mean R values across the 19 locations and for 9 sites identified as forested or close to forest are given in Table S3. Possible values of R span from -1 (perfect anti-correlation) to +1 (perfect correlation). Inclusion of an oxidized organic term in the particle formation rate increases the multi-site mean correlation coefficient R from 0.23 (for simulation B) to 0.37 (simulation C) and 0.40 (simulation D).

Additionally, we calculate the first aerosol indirect radiative forcing (RF) due to anthropogenic emissions, using nucleation mechanisms B, C and D. Changes to cloud

droplet number concentration are calculated using the parameterization from (*67*), as updated by (*68*) and (*69*). Following the methodology described in (*70*), the Edwards and Slingo radiative transfer model (*71*) is then used to calculate the radiative perturbation associated with the changes to cloud droplet number concentration since 1750. The range in the values obtained is 0.11 W m^{-2} (Table S4), approximately 10% of the magnitude of the indirect RF itself. The difference between the indirect RF obtained for the simulation using the Metzger et al. (*25*) mechanism, and our new mechanism, is 0.11 W m^{-2}; highlighting that there is uncertainty associated with the magnitude of the indirect RF even between two biogenically driven nucleation mechanisms due to their differing dependencies on H_2SO_4 and oxidant concentrations.

Comparison with rate coefficients derived from ambient measurements

The pseudo first order rate coefficient derived from the experiments is comparable to what has been derived from ambient data assuming a rate expression $J=k´[H_2SO_4]^2$. We can estimate the pseudo first order coefficient from $J=k´[H_2SO_4]^2=k_m[\text{BioOxOrg}][H_2SO_4]^2$ (so $k´=k_m[\text{BioOxOrg}]$). $[\text{BioOxOrg}]=k_{\alpha\text{-pin,OH}}[\alpha\text{-pin}][OH]/k_{CS}$. The α-pinene concentration varies a lot in the atmosphere, as does the condensation sink term k_{CS}. If we use $[\alpha\text{-pin}]=5\cdot10^9$ cm^{-3} (~200 pptv), $k_{CS}=10^{-3}$ s^{-1}, $[OH]=10^6$ cm^{-3}, $k_{\alpha\text{-pin,OH}}=10^{-11}\exp(444/T)$ and a measured $k_m=3.27\cdot10^{-21}$ cm^6 s^{-2}, then we get $k´=8\cdot10^{-13}$ cm^3 s^{-1}. Two studies have derived ranges of $k´$ from measured nucleation rates: Sihto et al. (2006) (*7*) estimated $k´=2\text{-}14\cdot10^{-13}$ cm^3 s^{-1} and Kuang et al. (2008) (*9*) estimated $k´=0.1\text{-}100\cdot10^{-13}$ cm^3 s^{-1} for a range of sites. Measured α-pinene

concentrations range from near zero to several hundred pptv (*33*), so our organic nucleation mechanism can comfortably span the range of derived values of *k´*.

Table S1. Cluster Gibbs free formation energies from monomers (x H_2SO_4 + y MBTCA → $((H_2SO_4)_x \cdot (MBTCA)_y)$ at 278K in kcal/mol.

Cluster	ΔG_{278K} (kcal/mol)
$H_2SO_4 \cdot MBTCA$	-14.40
$H_2SO_4 \cdot (MBTCA)_2$	-25.17
$(H_2SO_4)_2 \cdot MBTCA$	-23.13
$(H_2SO_4)_2 \cdot (MBTCA)_2$	-42.29
$(MBTCA)_2$	-7.03
$HSO_4^- \cdot MBTCA$	-34.02
$HSO_4^- \cdot H_2SO_4 \cdot MBTCA$	-50.83
$HSO_4^- \cdot (MBTCA)_2$	-45.25
$HSO_4^- \cdot H_2SO_4 \cdot (MBTCA)_2$	-67.02

Table S2: Observation sites used in comparison; taken from reference *57* [i.e. (*11*)].

Location		**Observation Period**	**Minimum cut-off diameter** (nm)
Hyytiälä	24.3°E, 61.9°N	2000-2004	3
Pallas	24.1°E, 68.0°N	2000-2004, 2007	10
Finokalia	25.7°E, 35.3°N	1997, 2006-2007	10
Hohenpeissenberg	11.0°E, 47.8°N	2006-2007	3
Melpitz	12.3°E, 51.2°N	1996-1997, 2003	3
Bondville	88.4°W, 40.1°N	1994-2007	14
Southern Great Plains	97.5°W, 36.6°N	1996-2007	10
Tomsk	85.1°E, 56.5°N	2005-2006	3
Listvyanka	104.9°E, 51.9°N	2005-2006	3
Harwell	359.0°E, 51.0°N	2000	10
Weybourne	1.1°E, 53.0°N	2005	10
India Himalaya	79.6°E, 29.4°N	2005-2008	10
Aspvreten	17.4°E, 58.8°N	2000-2006	10
Utö	21.4°E, 59.8°N	2003-2006	7
Värriö	29.6°E, 67.8°N	1998-2006	8
Thompson Farm	289.1°E, 43.1°N	2001-2009	7
Castle Springs	71.3°W, 43.7°N	2001-2008	7
Taunus Observatory	8.4°E, 50.2°N	2008-2009	10
Po Valley	11.6°E, 44.7°N	2002-2006	3

Table S3: Mean Pearson correlation coefficient, between multi-annual observed and simulated monthly-mean total particle concentration, across all 19 continental boundary layer locations, and those close to forested regions.

Simulation		**Pearson Correlation Coefficient (R)**	
		Mean over all sites	**Mean over *forested sites****
A	BHN	0.08	-0.09
B	BHN + $k_{ACT}[H_2SO_4]$	0.23	0.35
C	BHN + $k_{MET}[H_2SO_4][NucOrg]$	0.37	0.64
D	BHN + $k_m[H_2SO_4]^2[BioOxOrg]$	0.40-0.40	0.69 – 0.70

* Hyytiälä, Pallas, Melpitz, Tomsk, Lystvyanka, Harwell, Aspvreten, Värriö, Taunus Obs.

Table S4: First aerosol indirect radiative forcing due to anthropogenic emission changes (1750 to present).

Nucleation mechanism	**Indirect RF (W m^{-2})**	**Reference**
BHN + $k_{ACT}[H_2SO_4]$	-1.15	*(64)*
BHN + $k_{MET}[H_2SO_4][NucOrg]$	-1.04	*(25,70)*
BHN + $k_m[H_2SO_4]^2[BioOxOrg]$	-1.15	This study

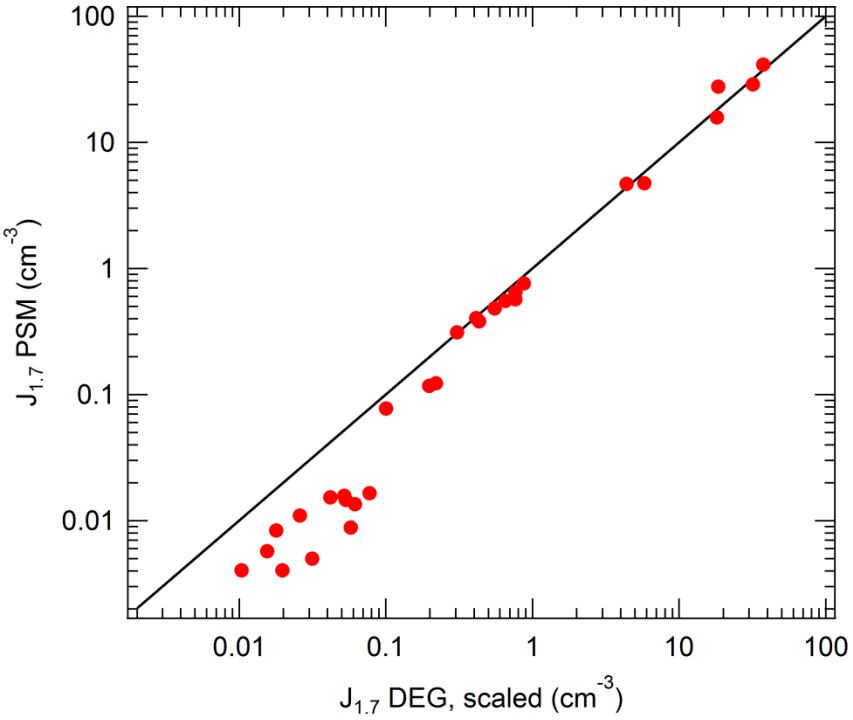

Fig. S1. Correlation of $J_{1.7}$ values determined either from the PSM or from the DEG CPC.

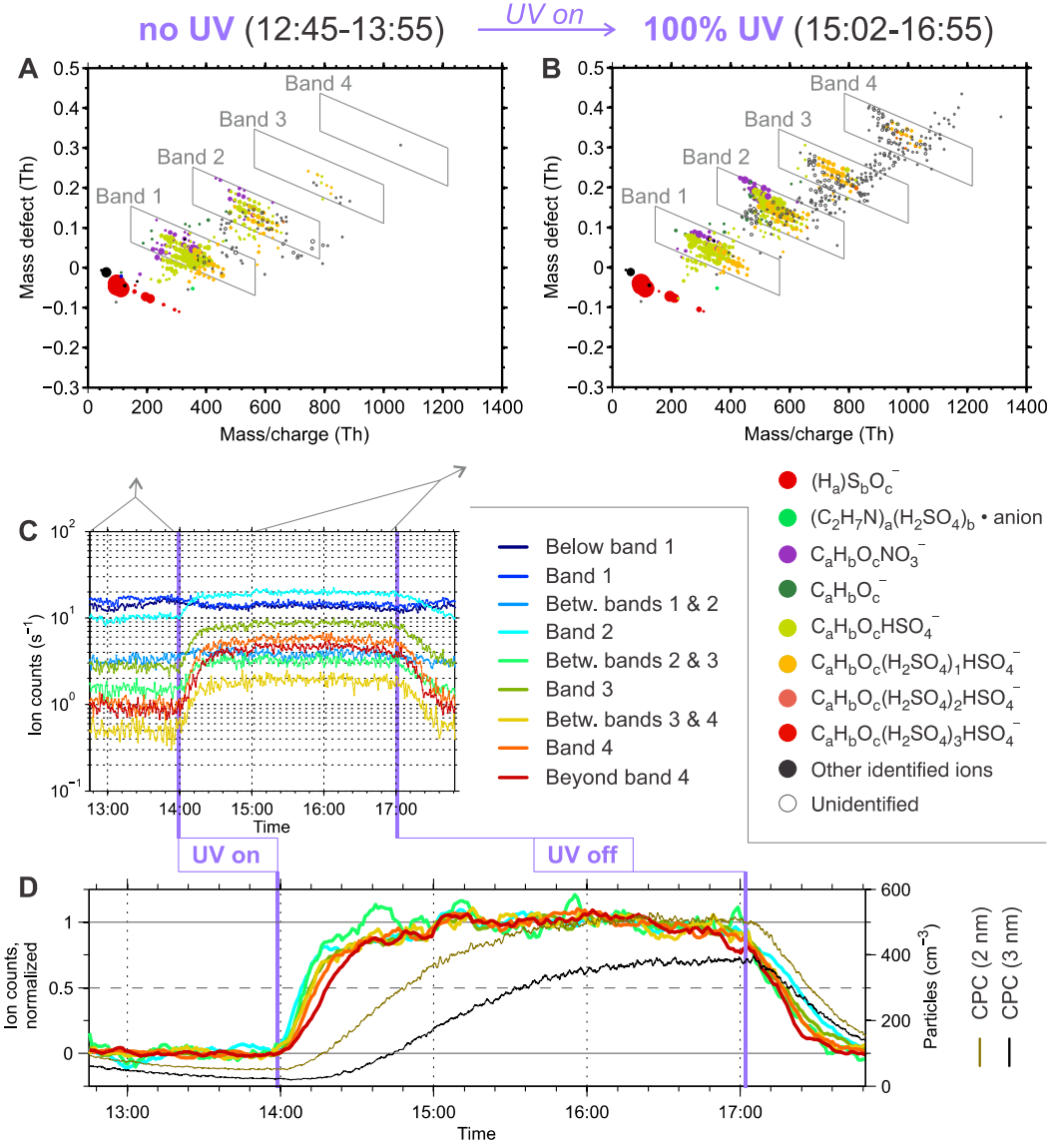

Fig. S2. Overview over a particle formation experiment initiated by the oxidation of SO_2 to H_2SO_4 and PD to BioOxOrg at 4.1 °C and 41% relative humidity. The measured precursor concentrations were [PD] = 16.4 ppbv and [SO_2] = 1.8 ppbv. Full UV illumination increased [H_2SO_4] to $2.0 \cdot 10^6$ cm^{-3} and [BioOxOrg] to $1.2 \cdot 10^8$ cm^{-3}. Before, most anions are single ions or clusters including a BioOxOrg containing 10 carbon atoms. These are found in band 1 (**A**). Upon increasing [BioOxOrg], more larger clusters form, which contain mainly oxidized organics including 20, 30, and 40 carbon atoms. Thus, these clusters are arranged in bands 2, 3, and 4 in the anions' mass defect diagram (**B**). This transition is initiated immediately upon full UV illumination (**C**). Normalizing the transitions of increasing of ion counts, here grouped by their masses, between zero and unity, shows how the larger ions grow from the second band onwards (**D**). Particle counts by CPCs are shown as well. Their cut-off diameters were 2 nm and 3 nm in mobility diameter. The obtained formation rate for 1.7 nm was 0.22 cm^{-3} s^{-1}.

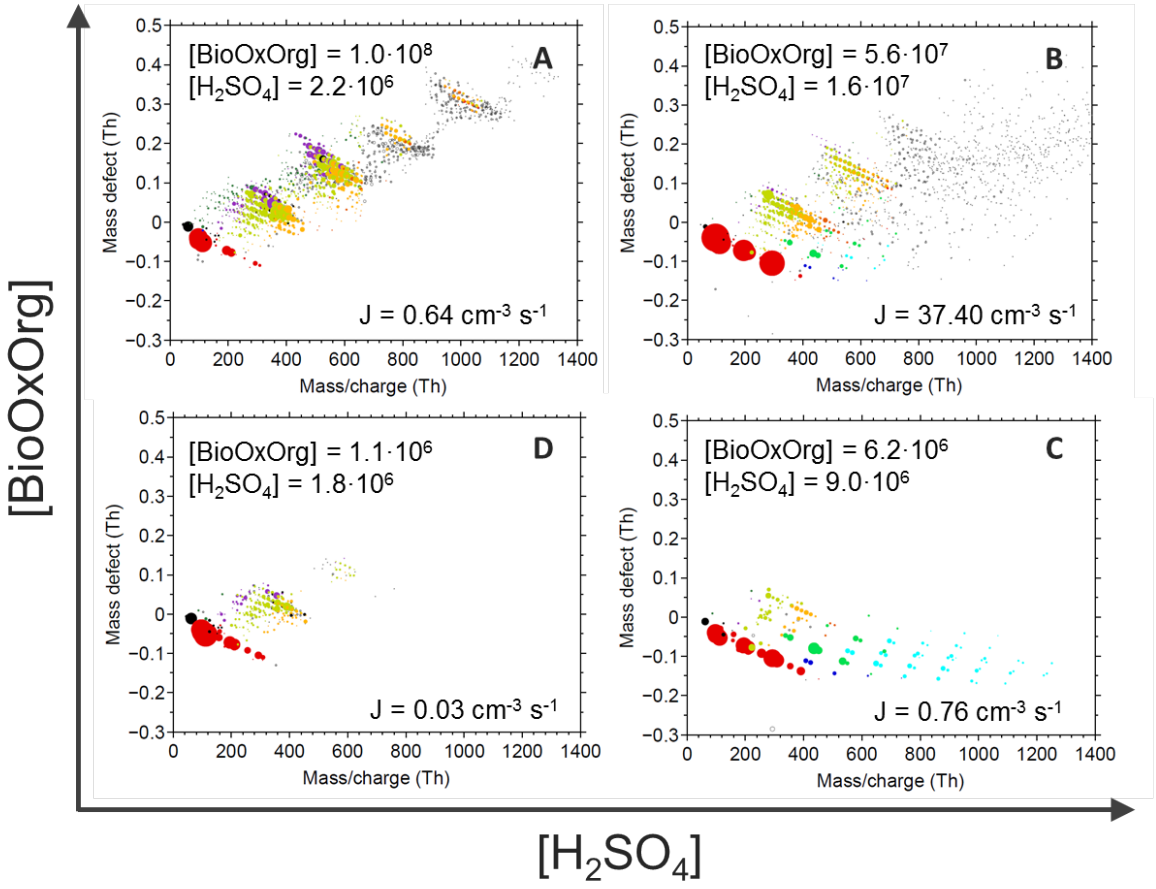

Fig. S3. APi-TOF mass defect plots for varying concentrations of H_2SO_4 and BioOxOrg. Nucleation rates as a function of [H_2SO_4] for panel A and B are part of Fig. 1B of the main text, while nucleation rates as a function of [BioOxOrg] for panels A and D are part of Fig. 1C of the main text. Panel C refers to an experiment with high [H_2SO_4] and low [BioOxOrg], it shows clusters similar to those observed during earlier experiments at the CLOUD chamber which investigated particle formation without organics (*16*). For the symbols' color coding, refer to the legend of Fig. S2. Additional colors used here are light blue for $(C_2H_7N)_a(NH_3)_b(H_2SO_4)_c\cdot$anion, and dark blue for $(NH_3)_a(H_2SO_4)_b$. The anion is either HSO_4^- or HSO_5^- (*16*).

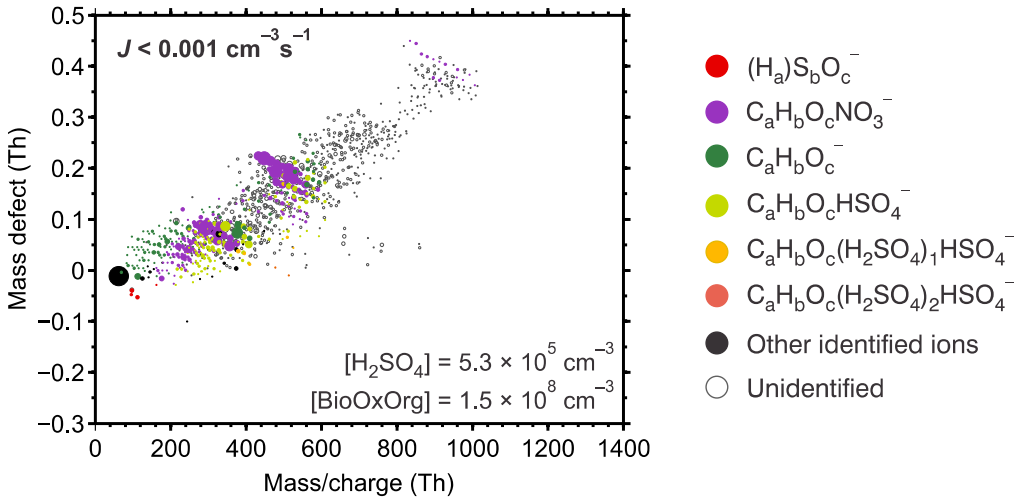

Fig. S4. APi-TOF mass defect plot for the lowest possible achievable concentration of sulfuric acid ($5.3 \cdot 10^5$ cm^{-3}), and high concentration of BioOxOrg ($1.5 \cdot 10^8$ cm^{-3}). Under these conditions, particle formation rates were close to 0 ($J < 0.001$ $cm^{-3}s^{-1}$), and BioOxOrg molecules are observed in clusters with the nitrate ion (NO_3^-) instead of HSO_4^-.

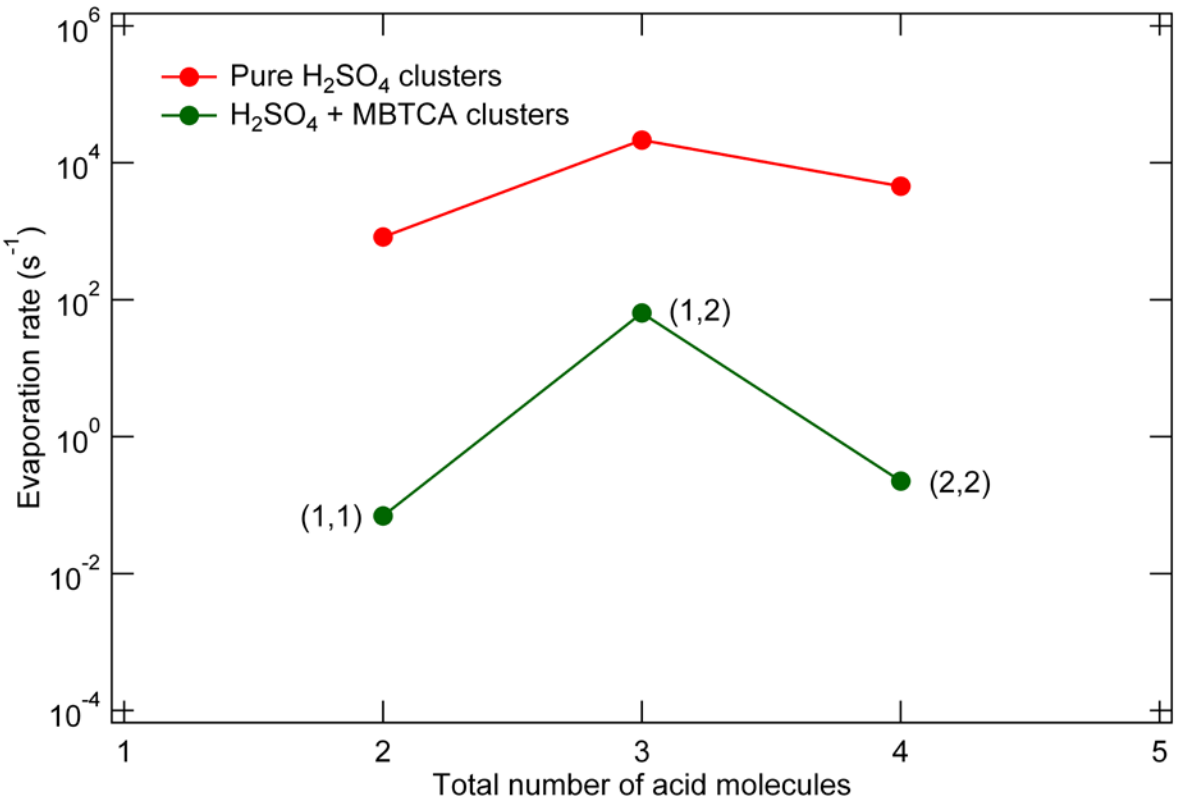

Figure S5. Evaporation rates (1/s) at 278K of $((H_2SO_4)_x \cdot (MBTCA)_y)$ (green) and pure H_2SO_4 (red) neutral clusters versus total number of molecules in the cluster. The numbers in parentheses indicate the composition (x,y) of the most stable cluster (H_2SO_4, MBTCA).

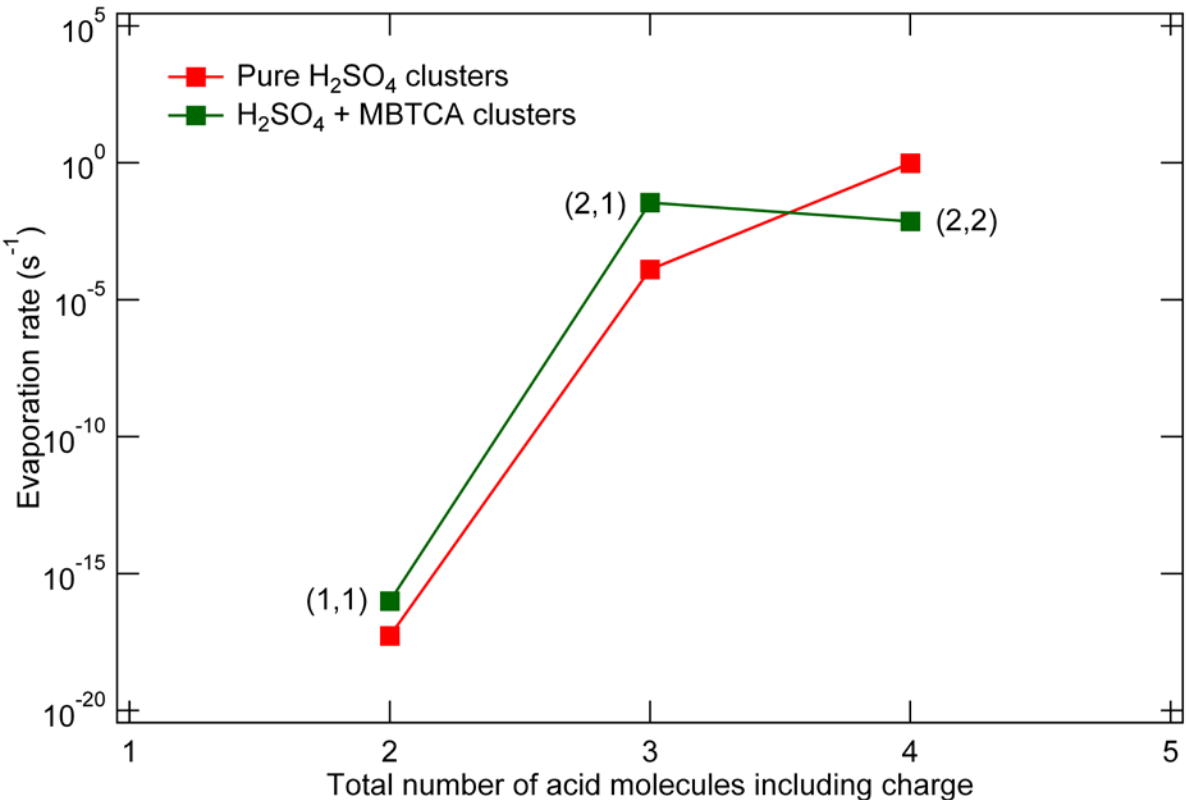

Figure S6. Evaporation rates (1/s) at 278K of $((H_2SO_4)_x \cdot (MBTCA)_y)$ (green) and pure H_2SO_4 (red) negatively charged clusters versus total number of molecules in the cluster. The numbers in parentheses indicate the composition (x,y) of the most stable cluster (H_2SO_4/ HSO_4^-, MBTCA).

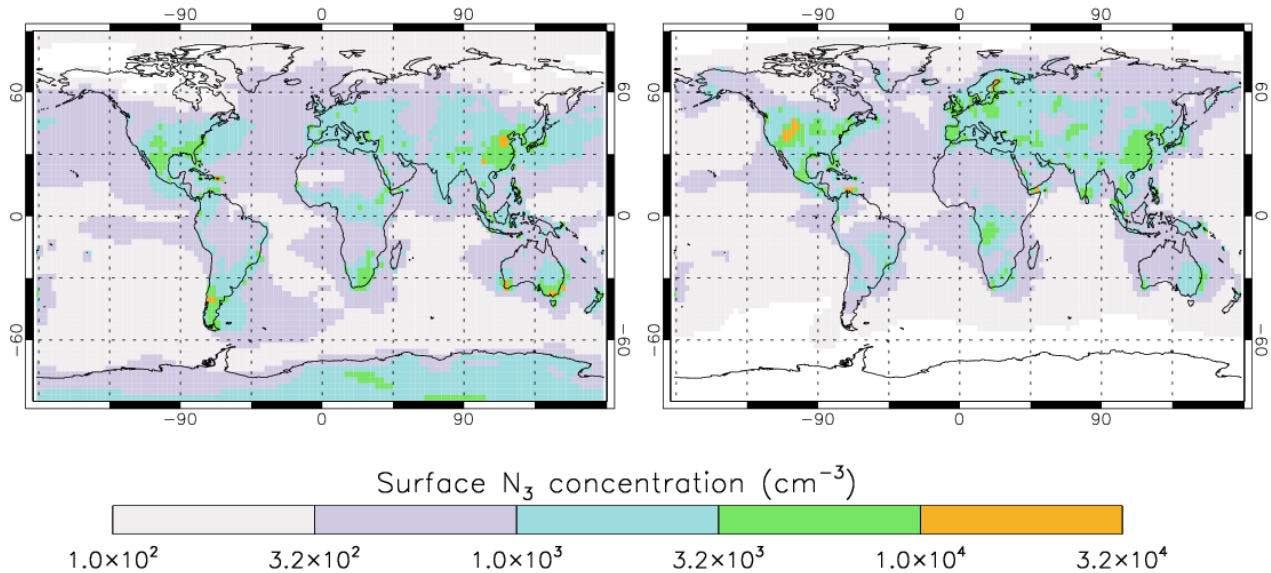

Figure S7. Simulated monthly mean particle number concentrations (diameter greater than 3 nm) per cm^3 for January (left) and June (right), when the parameterized nucleation rate involving organics (Eq. S6) and BHN occurs throughout the atmosphere.

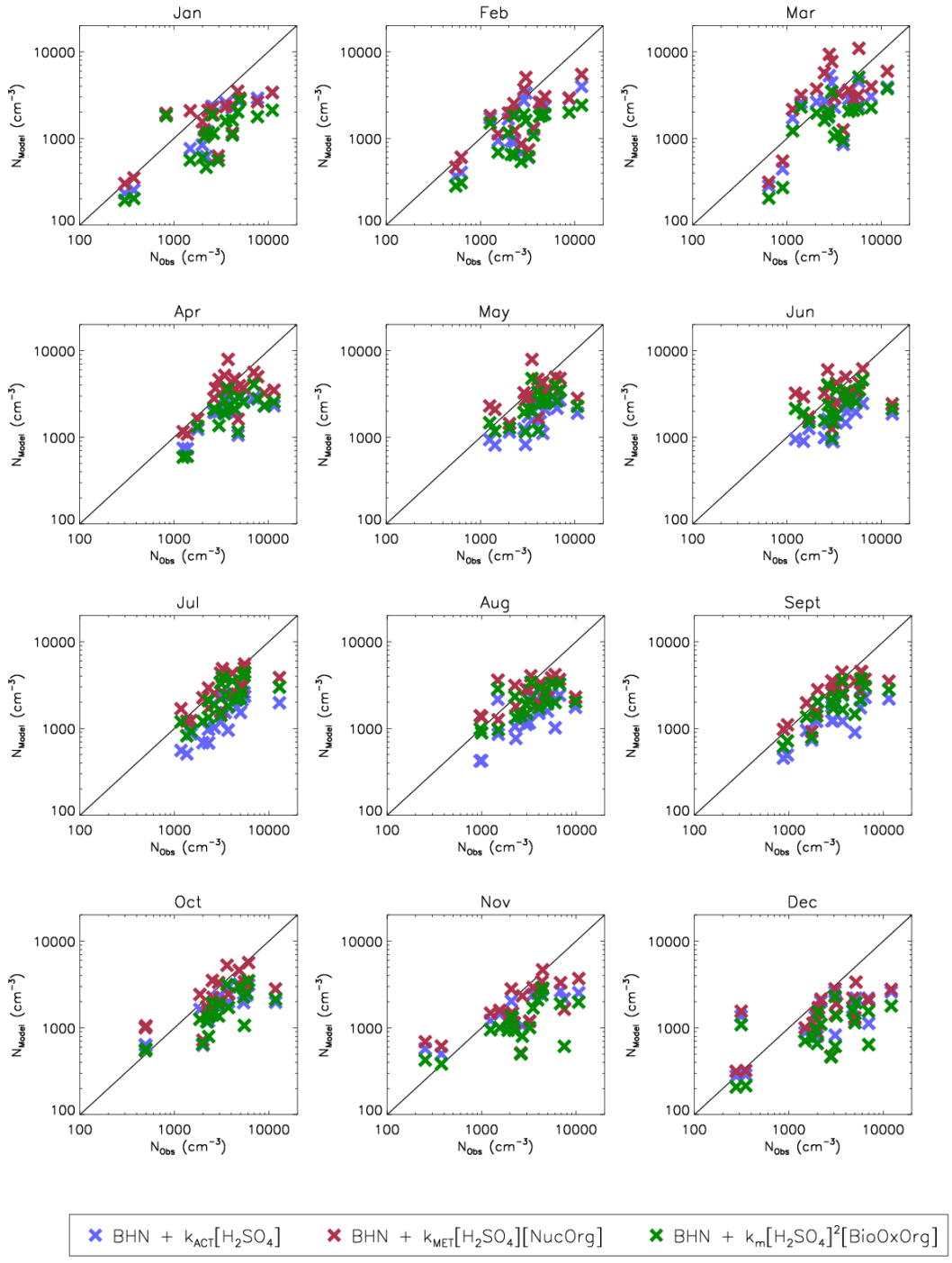

Figure S8. Model versus observation comparison in total particle concentration (at the relevant particle size for each location) for each month.

References and Notes

1. Intergovernmental Panel on Climate Change, *Climate Change 2007: The Physical Science Basis. Contribution of Working Group I to the Fourth Assessment Report of the Intergovernmental Panel on Climate Change*, S. Solomon *et al*., Eds. (Cambridge Univ. Press, New York, 2007).

2. M. Kulmala, H. Vehkamäki, T. Petäjä, M. Dal Maso, A. Lauri, V.-M. Kerminen, W. Birmili, P. H. McMurry, Formation and growth rates of ultrafine atmospheric particles: A review of observations. *J. Aerosol Sci.* **35**, 143–176 (2004). doi:10.1016/j.jaerosci.2003.10.003

3. F. Yu, G. Luo, Simulation of particle size distribution with a global aerosol model: Contribution of nucleation to aerosol and CCN number concentrations. *Atmos. Chem. Phys.* **9**, 7691–7710 (2009). doi:10.5194/acp-9-7691-2009

4. J. Merikanto, D. V. Spracklen, G. W. Mann, S. J. Pickering, K. S. Carslaw, Impact of nucleation on global CCN. *Atmos. Chem. Phys.* **9**, 8601–8616 (2009). doi:10.5194/acp-9-8601-2009

5. R. Zhang, A. Khalizov, L. Wang, M. Hu, W. Xu, Nucleation and growth of nanoparticles in the atmosphere. *Chem. Rev.* **112**, 1957–2011 (2012). Medline doi:10.1021/cr2001756

6. R. J. Weber, J. J. Marti, P. H. McMurry, F. L. Eisele, D. J. Tanner, A. Jefferson, Measurements of new particle formation and ultrafine particle growth rates at a clean continental site. *J. Geophys. Res.* **102**, 4375 (1997). doi:10.1029/96JD03656

7. S. L. Sihto, M. Kulmala, V.-M. Kerminen, M. Dal Maso, T. Petäjä, I. Riipinen, H. Korhonen, F. Arnold, R. Janson, M. Boy, A. Laaksonen, K. E. J. Lehtinen, Atmospheric sulphuric acid and aerosol formation: Implications from atmospheric measurements for nucleation and early growth mechanisms. *Atmos. Chem. Phys.* **6**, 4079–4091 (2006). doi:10.5194/acp-6-4079-2006

8. I. Riipinen, S.-L. Sihto, M. Kulmala, F. Arnold, M. Dal Maso, W. Birmili, K. Saarnio, K. Teinilä, V.-M. Kerminen, A. Laaksonen, K. E. J. Lehtinen, Connections between atmospheric sulphuric acid and new particle formation during QUEST III–IV campaigns in Heidelberg and Hyytiälä. *Atmos. Chem. Phys.* **7**, 1899–1914 (2007). doi:10.5194/acp-7-1899-2007

9. C. Kuang, P. H. McMurry, A. V. McCormick, F. L. Eisele, Dependence of nucleation rates on sulfuric acid vapor concentration in diverse atmospheric locations. *J. Geophys. Res.* **113**, D10209 (2008). doi:10.1029/2007JD009253

10. R. J. Weber, J. J. Marti, P. H. McMURRY, F. L. Eisele, D. J. Tanner, A. Jefferson, Measured atmospheric new particle formation rates: Implications for nucleation mechanisms. *Chem. Eng. Commun.* **151**, 53–64 (1996). doi:10.1080/00986449608936541

11. D. V. Spracklen, K. S. Carslaw, J. Merikanto, G. W. Mann, C. L. Reddington, S. Pickering, J. A. Ogren, E. Andrews, U. Baltensperger, E. Weingartner, M. Boy, M. Kulmala, L. Laakso, H. Lihavainen, N. Kivekäs, M. Komppula, N.

Mihalopoulos, G. Kouvarakis, S. G. Jennings, C. O'Dowd, W. Birmili, A. Wiedensohler, R. Weller, J. Gras, P. Laj, K. Sellegri, B. Bonn, R. Krejci, A. Laaksonen, A. Hamed, A. Minikin, R. M. Harrison, R. Talbot, J. Sun, Explaining global surface aerosol number concentrations in terms of primary emissions and particle formation. *Atmos. Chem. Phys.* **10**, 4775–4793 (2010). doi:10.5194/acp-10-4775-2010

12. R. J. Weber, P. H. McMurry, L. Mauldin, D. J. Tanner, F. L. Eisele, F. J. Brechtel, S. M. Kreidenweis, G. L. Kok, R. D. Schillawski, D. Baumgardner, A study of new particle formation and growth involving biogenic and trace gas species measured during ACE 1. *J. Geophys. Res.* **103**, 16385 (1998). doi:10.1029/97JD02465

13. F. L. Eisele, E. R. Lovejoy, E. Kosciuch, K. F. Moore, R. L. Mauldin III, J. N. Smith, P. H. McMurry, K. Iida, Negative atmospheric ions and their potential role in ion-induced nucleation. *J. Geophys. Res.* **111**, D04305 (2006). doi:10.1029/2005JD006568

14. P. Paasonen, T. Nieminen, E. Asmi, H. E. Manninen, T. Petäjä, C. Plass-Dülmer, H. Flentje, W. Birmili, A. Wiedensohler, U. Hõrrak, A. Metzger, A. Hamed, A. Laaksonen, M. C. Facchini, V.-M. Kerminen, M. Kulmala, On the roles of sulphuric acid and low-volatility organic vapours in the initial steps of atmospheric new particle formation. *Atmos. Chem. Phys.* **10**, 11223–11242 (2010). doi:10.5194/acp-10-11223-2010

15. M. Kulmala, J. Kontkanen, H. Junninen, K. Lehtipalo, H. E. Manninen, T. Nieminen, T. Petäjä, M. Sipilä, S. Schobesberger, P. Rantala, A. Franchin, T. Jokinen, E. Järvinen, M. Äijälä, J. Kangasluoma, J. Hakala, P. P. Aalto, P. Paasonen, J. Mikkilä, J. Vanhanen, J. Aalto, H. Hakola, U. Makkonen, T. Ruuskanen, R. L. Mauldin 3rd, J. Duplissy, H. Vehkamäki, J. Bäck, A. Kortelainen, I. Riipinen, T. Kurtén, M. V. Johnston, J. N. Smith, M. Ehn, T. F. Mentel, K. E. Lehtinen, A. Laaksonen, V. M. Kerminen, D. R. Worsnop, Direct observations of atmospheric aerosol nucleation. *Science* **339**, 943–946 (2013). Medline doi:10.1126/science.1227385

16. J. Kirkby, J. Curtius, J. Almeida, E. Dunne, J. Duplissy, S. Ehrhart, A. Franchin, S. Gagné, L. Ickes, A. Kürten, A. Kupc, A. Metzger, F. Riccobono, L. Rondo, S. Schobesberger, G. Tsagkogeorgas, D. Wimmer, A. Amorim, F. Bianchi, M. Breitenlechner, A. David, J. Dommen, A. Downard, M. Ehn, R. C. Flagan, S. Haider, A. Hansel, D. Hauser, W. Jud, H. Junninen, F. Kreissl, A. Kvashin, A. Laaksonen, K. Lehtipalo, J. Lima, E. R. Lovejoy, V. Makhmutov, S. Mathot, J. Mikkilä, P. Minginette, S. Mogo, T. Nieminen, A. Onnela, P. Pereira, T. Petäjä, R. Schnitzhofer, J. H. Seinfeld, M. Sipilä, Y. Stozhkov, F. Stratmann, A. Tomé, J. Vanhanen, Y. Viisanen, A. Vrtala, P. E. Wagner, H. Walther, E. Weingartner, H. Wex, P. M. Winkler, K. S. Carslaw, D. R. Worsnop, U. Baltensperger, M. Kulmala, Role of sulphuric acid, ammonia and galactic cosmic rays in atmospheric aerosol nucleation. *Nature* **476**, 429–433 (2011). Medline doi:10.1038/nature10343

17. R. Zhang, I. Suh, J. Zhao, D. Zhang, E. C. Fortner, X. Tie, L. T. Molina, M. J. Molina, Atmospheric new particle formation enhanced by organic acids. *Science* **304**, 1487–1490 (2004). Medline doi:10.1126/science.1095139

18. R. Zhang, L. Wang, A. F. Khalizov, J. Zhao, J. Zheng, R. L. McGraw, L. T. Molina, Formation of nanoparticles of blue haze enhanced by anthropogenic pollution. *Proc. Natl. Acad. Sci. U.S.A.* **106**, 17650–17654 (2009). Medline doi:10.1073/pnas.0910125106

19. S. M. Ball, D. R. Hanson, F. L. Eisele, P. H. McMurry, Laboratory studies of particle nucleation: Initial results for H_2SO_4, H_2O, and NH_3 vapors. *J. Geophys. Res.* **104**, 23709 (1999). doi:10.1029/1999JD900411

20. L. H. Young, D. R. Benson, F. R. Kameel, J. R. Pierce, H. Junninen, M. Kulmala, S.-H. Lee, Laboratory studies of H_2SO_4/H_2O binary homogeneous nucleation from the SO_2+OH reaction: Evaluation of the experimental setup and preliminary results. *Atmos. Chem. Phys.* **8**, 4997–5016 (2008). doi:10.5194/acp-8-4997-2008

21. A. Laaksonen, M. Kulmala, T. Berndt, F. Stratmann, S. Mikkonen, A. Ruuskanen, K. E. J. Lehtinen, M. Dal Maso, P. Aalto, T. Petäjä, I. Riipinen, S.-L. Sihto, R. Janson, F. Arnold, M. Hanke, J. Ücker, B. Umann, K. Sellegri, C. D. O'Dowd, Y. Viisanen, SO_2 oxidation products other than H_2SO_4 as a trigger of new particle formation. Part 2: Comparison of ambient and laboratory measurements, and atmospheric implications. *Atmos. Chem. Phys.* **8**, 7255–7264 (2008). doi:10.5194/acp-8-7255-2008

22. A. Sorokin, F. Arnold, Laboratory study of cluster ions formation in H_2SO_4–H_2O system: Implications for threshold concentration of gaseous H_2SO_4 and ion-induced nucleation kinetics. *Atmos. Environ.* **41**, 3740–3747 (2007). doi:10.1016/j.atmosenv.2007.01.017

23. M. Chen, M. Titcombe, J. Jiang, C. Jen, C. Kuang, M. L. Fischer, F. L. Eisele, J. I. Siepmann, D. R. Hanson, J. Zhao, P. H. McMurry, Acid-base chemical reaction model for nucleation rates in the polluted atmospheric boundary layer. *Proc. Natl. Acad. Sci. U.S.A.* **109**, 18713–18718 (2012). Medline doi:10.1073/pnas.1210285109

24. J. Almeida, S. Schobesberger, A. Kürten, I. K. Ortega, O. Kupiainen-Määttä, A. P. Praplan, A. Adamov, A. Amorim, F. Bianchi, M. Breitenlechner, A. David, J. Dommen, N. M. Donahue, A. Downard, E. Dunne, J. Duplissy, S. Ehrhart, R. C. Flagan, A. Franchin, R. Guida, J. Hakala, A. Hansel, M. Heinritzi, H. Henschel, T. Jokinen, H. Junninen, M. Kajos, J. Kangasluoma, H. Keskinen, A. Kupc, T. Kurtén, A. N. Kvashin, A. Laaksonen, K. Lehtipalo, M. Leiminger, J. Leppä, V. Loukonen, V. Makhmutov, S. Mathot, M. J. McGrath, T. Nieminen, T. Olenius, A. Onnela, T. Petäjä, F. Riccobono, I. Riipinen, M. Rissanen, L. Rondo, T. Ruuskanen, F. D. Santos, N. Sarnela, S. Schallhart, R. Schnitzhofer, J. H. Seinfeld, M. Simon, M. Sipilä, Y. Stozhkov, F. Stratmann, A. Tomé, J. Tröstl, G. Tsagkogeorgas, P. Vaattovaara, Y. Viisanen, A. Virtanen, A. Vrtala, P. E. Wagner, E. Weingartner, H. Wex, C. Williamson, D. Wimmer, P. Ye, T. Yli-Juuti, K. S. Carslaw, M. Kulmala, J. Curtius, U. Baltensperger, D. R. Worsnop, H.

Vehkamäki, J. Kirkby, Molecular understanding of sulphuric acid-amine particle nucleation in the atmosphere. *Nature* **502**, 359–363 (2013). Medline doi:10.1038/nature12663

25. A. Metzger, B. Verheggen, J. Dommen, J. Duplissy, A. S. Prevot, E. Weingartner, I. Riipinen, M. Kulmala, D. V. Spracklen, K. S. Carslaw, U. Baltensperger, Evidence for the role of organics in aerosol particle formation under atmospheric conditions. *Proc. Natl. Acad. Sci. U.S.A.* **107**, 6646–6651 (2010). Medline doi:10.1073/pnas.0911330107

26. F. Riccobono, L. Rondo, M. Sipilä, P. Barmet, J. Curtius, J. Dommen, M. Ehn, S. Ehrhart, M. Kulmala, A. Kürten, J. Mikkilä, P. Paasonen, T. Petäjä, E. Weingartner, U. Baltensperger, Contribution of sulfuric acid and oxidized organic compounds to particle formation and growth. *Atmos. Chem. Phys.* **12**, 9427–9439 (2012). doi:10.5194/acp-12-9427-2012

27. M. Sipilä, T. Berndt, T. Petäjä, D. Brus, J. Vanhanen, F. Stratmann, J. Patokoski, R. L. Mauldin 3rd, A. P. Hyvärinen, H. Lihavainen, M. Kulmala, The role of sulfuric acid in atmospheric nucleation. *Science* **327**, 1243–1246 (2010). Medline doi:10.1126/science.1180315

28. Materials and methods are available as supporting materials on *Science* Online.

29. D. W. Oxtoby, D. Kashchiev, A general relation between the nucleation work and the size of the nucleus in multicomponent nucleation. *J. Chem. Phys.* **100**, 7665–7671 (1994). doi:10.1063/1.466859

30. S. Ehrhart, J. Curtius, Influence of aerosol lifetime on the interpretation of nucleation experiments with respect to the first nucleation theorem. *Atmos. Chem. Phys.* **13**, 11465–11471 (2013). doi:10.5194/acp-13-11465-2013

31. M. Ehn, H. Junninen, T. Petäjä, T. Kurtén, V.-M. Kerminen, S. Schobesberger, H. E. Manninen, I. K. Ortega, H. Vehkamäki, M. Kulmala, D. R. Worsnop, Composition and temporal behavior of ambient ions in the boreal forest. *Atmos. Chem. Phys.* **10**, 8513–8530 (2010). doi:10.5194/acp-10-8513-2010

32. S. Schobesberger, H. Junninen, F. Bianchi, G. Lönn, M. Ehn, K. Lehtipalo, J. Dommen, S. Ehrhart, I. K. Ortega, A. Franchin, T. Nieminen, F. Riccobono, M. Hutterli, J. Duplissy, J. Almeida, A. Amorim, M. Breitenlechner, A. J. Downard, E. M. Dunne, R. C. Flagan, M. Kajos, H. Keskinen, J. Kirkby, A. Kupc, A. Kürten, T. Kurtén, A. Laaksonen, S. Mathot, A. Onnela, A. P. Praplan, L. Rondo, F. D. Santos, S. Schallhart, R. Schnitzhofer, M. Sipilä, A. Tomé, G. Tsagkogeorgas, H. Vehkamäki, D. Wimmer, U. Baltensperger, K. S. Carslaw, J. Curtius, A. Hansel, T. Petäjä, M. Kulmala, N. M. Donahue, D. R. Worsnop, Molecular understanding of atmospheric particle formation from sulfuric acid and large oxidized organic molecules. *Proc. Natl. Acad. Sci. U.S.A.* **110**, 17223–17228 (2013). Medline doi:10.1073/pnas.1306973110

33. H. Hakola, H. Hellen, M. Hemmila, J. Rinne, M. Kulmala, In situ measurements of volatile organic compounds in a boreal forest. *Atmos. Chem. Phys.* **12**, 11665–11678 (2012). doi:10.5194/acp-12-11665-2012

34. D. V. Spracklen, K. J. Pringle, K. S. Carslaw, M. P. Chipperfield, G. W. Mann, A global off-line model of size-resolved aerosol microphysics: I. Model development and prediction of aerosol properties. *Atmos. Chem. Phys.* **5**, 2227–2252 (2005). doi:10.5194/acp-5-2227-2005

35. G. W. Mann, K. S. Carslaw, D. V. Spracklen, D. A. Ridley, P. T. Manktelow, M. P. Chipperfield, S. J. Pickering, C. E. Johnson, Description and evaluation of GLOMAP-mode: A modal global aerosol microphysics model for the UKCA composition-climate model. *Geosci. Model Dev.* **3**, 519–551 (2010). doi:10.5194/gmd-3-519-2010

36. A. Guenther, C. N. Hewitt, D. Erickson, R. Fall, C. Geron, T. Graedel, P. Harley, L. Klinger, M. Lerdau, W. A. Mckay, T. Pierce, B. Scholes, R. Steinbrecher, R. Tallamraju, J. Taylor, P. Zimmerman, A global model of natural volatile organic compound emissions. *J. Geophys. Res.* **100**, 8873–8892 (1995). doi:10.1029/94JD02950

37. L. A. Lee, K. J. Pringle, C. L. Reddington, G. W. Mann, P. Stier, D. V. Spracklen, J. R. Pierce, K. S. Carslaw, The magnitude and causes of uncertainty in global model simulations of cloud condensation nuclei. *Atmos. Chem. Phys.* **13**, 8879–8914 (2013). doi:10.5194/acp-13-8879-2013

38. K. S. Carslaw, L. A. Lee, C. L. Reddington, G. W. Mann, K. J. Pringle, The magnitude and sources of uncertainty in global aerosol. *Faraday Discuss.* **165**, 495–512 (2013). Medline doi:10.1039/c3fd00043e

39. A. B. Nadykto, F. Q. Yu, Strong hydrogen bonding between atmospheric nucleation precursors and common organics. *Chem. Phys. Lett.* **435**, 14–18 (2007). doi:10.1016/j.cplett.2006.12.050

40. T. Kurtén, V. Loukonen, H. Vehkamäki, M. Kulmala, Amines are likely to enhance neutral and ion-induced sulfuric acid-water nucleation in the atmosphere more effectively than ammonia. *Atmos. Chem. Phys.* **8**, 4095–4103 (2008). doi:10.5194/acp-8-4095-2008

41. N. M. Donahue, E. R. Trump, J. R. Pierce, I. Riipinen, Theoretical constraints on pure vapor-pressure driven condensation of organics to ultrafine particles. *Geophys. Res. Lett.* **38**, L16801 (2011). doi:10.1029/2011GL048115

42. N. M. Donahue, K. M. Henry, T. F. Mentel, A. Kiendler-Scharr, C. Spindler, B. Bohn, T. Brauers, H. P. Dorn, H. Fuchs, R. Tillmann, A. Wahner, H. Saathoff, K. H. Naumann, O. Möhler, T. Leisner, L. Müller, M. C. Reinnig, T. Hoffmann, K. Salo, M. Hallquist, M. Frosch, M. Bilde, T. Tritscher, P. Barmet, A. P. Praplan, P. F. DeCarlo, J. Dommen, A. S. Prévôt, U. Baltensperger, Aging of biogenic secondary organic aerosol via gas-phase OH radical reactions. *Proc. Natl. Acad. Sci. U.S.A.* **109**, 13503–13508 (2012). Medline doi:10.1073/pnas.1115186109

43. R. Schnitzhofer, A. Metzger, M. Breitenlechner, W. Jud, M. Heinritzi, L.-P. De Menezes, J. Duplissy, R. Guida, S. Haider, J. Kirkby, S. Mathot, P. Minginette, A. Onnela, H. Walther, A. Wasem, A. Hansel, Characterisation of organic contaminants in the CLOUD chamber at CERN. *Atmos. Meas. Tech. Discuss.* **6**, 7709–7734 (2013). doi:10.5194/amtd-6-7709-2013

44. A. Kürten, L. Rondo, S. Ehrhart, J. Curtius, Performance of a corona ion source for measurement of sulfuric acid by chemical ionization mass spectrometry. *Atmos. Meas. Tech.* **4**, 437–443 (2011). doi:10.5194/amt-4-437-2011

45. M. Graus, M. Müller, A. Hansel, High resolution PTR-TOF: Quantification and formula confirmation of VOC in real time. *J. Am. Soc. Mass Spectrom.* **21**, 1037–1044 (2010). Medline doi:10.1016/j.jasms.2010.02.006

46. A. P. Praplan, F. Bianchi, J. Dommen, U. Baltensperger, Dimethylamine and ammonia measurements with ion chromatography during the CLOUD4 campaign. *Atmos. Meas. Tech.* **5**, 2161–2167 (2012). doi:10.5194/amt-5-2161-2012

47. H. Junninen, M. Ehn, T. Petäjä, L. Luosujärvi, T. Kotiaho, R. Kostiainen, U. Rohner, M. Gonin, K. Fuhrer, M. Kulmala, D. R. Worsnop, A high-resolution mass spectrometer to measure atmospheric ion composition. *Atmos. Meas. Tech.* **3**, 1039–1053 (2010). doi:10.5194/amt-3-1039-2010

48. J. Vanhanen, J. Mikkilä, K. Lehtipalo, M. Sipilä, H. E. Manninen, E. Siivola, T. Petäjä, M. Kulmala, Particle Size Magnifier for nano-CN detection. *Aerosol Sci. Technol.* **45**, 533–542 (2011). doi:10.1080/02786826.2010.547889

49. K. Iida, M. R. Stolzenburg, P. H. McMurry, Effect of working fluid on sub-2 nm particle detection with a laminar flow ultrafine condensation particle counter. *Aerosol Sci. Technol.* **43**, 81–96 (2009). doi:10.1080/02786820802488194

50. D. Wimmer, K. Lehtipalo, A. Franchin, J. Kangasluoma, F. Kreissl, A. Kürten, A. Kupc, A. Metzger, J. Mikkilä, T. Petäjä, F. Riccobono, J. Vanhanen, M. Kulmala, J. Curtius, Performance of diethylene glycol based particle counters in the sub 3 nm size range. *Atmos. Meas. Tech.* **6**, 1793–1804 (2013). doi:10.5194/amt-6-1793-2013

51. V.-M. Kerminen, M. Kulmala, M. Analytical formulae connecting the “real” and the “apparent” nucleation rate and the nuclei number concentration for atmospheric nucleation events. *J. Aerosol Sci.* **33**, 609–622 (2002). doi:10.1016/S0021-8502(01)00194-X

52. O. Welz, J. D. Savee, D. L. Osborn, S. S. Vasu, C. J. Percival, D. E. Shallcross, C. A. Taatjes, Direct kinetic measurements of Criegee intermediate (CH_2OO) formed by reaction of CH_2I with O_2. *Science* **335**, 204–207 (2012). Medline doi:10.1126/science.1213229

53. D. R. Hanson, F. Eisele, Diffusion of H_2SO_4 in humidified nitrogen: Hydrated H_2SO_4. *J. Phys. Chem. A* **104**, 1715–1719 (2000). doi:10.1021/jp993622j

54. K. Ortega, O. Kupiainen, T. Kurtén, T. Olenius, O. Wilkman, M. J. McGrath, V. Loukonen, H. Vehkamäki, From quantum chemical formation free energies to evaporation rates. *Atmos. Chem. Phys.* **12**, 225–235 (2012). doi:10.5194/acp-12-225-2012

55. M. J. Frisch *et al.*, GAUSSIAN 09, Revision A.1, Gaussian Inc. Wallingford, CT (2009).

56. A. D. Becke, Density-functional thermochemistry. III. The role of exact exchange. *J. Chem. Phys.* **98**, 5648 (1993). doi:10.1063/1.464913

57. A. Montgomery Jr., M. J. Frisch, J. W. Ochterski, G. A. Petersson, A complete basis set model chemistry. VI. Use of density functional geometries and frequencies. *J. Chem. Phys.* **110**, 2822 (1999). doi:10.1063/1.477924

58. R. Ahlrichs, M. Bär, M. Häser, H. Horn, C. Kölmel, Electronic structure calculations on workstation computers: The program system turbomole. *Chem. Phys. Lett.* **162**, 165–169 (1989). doi:10.1016/0009-2614(89)85118-8

59. C. Hättig, F. Weigend, CC2 excitation energy calculations on large molecules using the resolution of the identity approximation. *J. Chem. Phys.* **113**, 5154 (2000). doi:10.1063/1.1290013

60. T. H. Dunning Jr., K. A. Peterson, A. K. Wilson, Gaussian basis sets for use in correlated molecular calculations. X. The atoms aluminum through argon revisited. *J. Chem. Phys.* **114**, 9244 (2001). doi:10.1063/1.1367373

61. J. D. Crounse, L. B. Nielsen, S. Jørgensen, H. G. Kjaergaard, P. O. Wennberg, Autoxidation of organic compounds in the atmosphere. *J. Phys. Chem. Lett.* **4**, 3513–3520 (2013). doi:10.1021/jz4019207

62. M. Ehn, J. A. Thornton, E. Kleist, M. Sipilä, H. Junninen, I. Pullinen, M. Springer, F. Rubach, R. Tillmann, B. Lee, F. Lopez-Hilfiker, S. Andres, I. H. Acir, M. Rissanen, T. Jokinen, S. Schobesberger, J. Kangasluoma, J. Kontkanen, T. Nieminen, T. Kurtén, L. B. Nielsen, S. Jørgensen, H. G. Kjaergaard, M. Canagaratna, M. D. Maso, T. Berndt, T. Petäjä, A. Wahner, V. M. Kerminen, M. Kulmala, D. R. Worsnop, J. Wildt, T. F. Mentel, A large source of low-volatility secondary organic aerosol. *Nature* **506**, 476–479 (2014). Medline doi:10.1038/nature13032

63. M. P. Chipperfield, New version of the TOMCAT/SLIMCAT off-line chemical transport model: Intercomparison of stratospheric tracer experiments. *Q. J. R. Meteorol. Soc.* **132**, 1179–1203 (2006). doi:10.1256/qj.05.51

64. M. Kulmala, K. E. J. Lehtinen, A. Laaksonen, Cluster activation theory as an explanation of the linear dependence between formation rate of 3nm particles and sulphuric acid concentration. *Atmos. Chem. Phys.* **6**, 787–793 (2006). doi:10.5194/acp-6-787-2006

65. R. Atkinson, D. L. Baulch, R. A. Cox, J. N. Crowley, R. F. Hampson, R. G. Hynes, M. E. Jenkin, M. J. Rossi, J. Troe; IUPAC Subcommittee, Evaluated kinetic and photochemical data for atmospheric chemistry: Volume II - gas phase reactions of organic species. *Atmos. Chem. Phys.* **6**, 3625–4055 (2006). doi:10.5194/acp-6-3625-2006

66. G. W. Mann, K. S. Carslaw, D. A. Ridley, D. V. Spracklen, K. J. Pringle, J. Merikanto, H. Korhonen, J. P. Schwarz, L. A. Lee, P. T. Manktelow, M. T. Woodhouse, A. Schmidt, T. J. Breider, K. M. Emmerson, C. L. Reddington, M. P. Chipperfield, S. J. Pickering, Intercomparison of modal and sectional aerosol microphysics representations within the same 3-D global chemical transport

model. *Atmos. Chem. Phys.* **12**, 4449–4476 (2012). doi:10.5194/acp-12-4449-2012

67. A. Nenes, J. H. Seinfeld, Parameterization of cloud droplet formation in global climate models. *J. Geophys. Res.* **108**, 4415 (2003). doi:10.1029/2002JD002911

68. C. Fountoukis, A. Nenes, Continued development of a cloud droplet formation parameterization for global climate models. *J. Geophys. Res.* **110**, D11212 (2005). doi:10.1029/2004JD005591

69. D. Barahona, R. E. L. West, P. Stier, S. Romakkaniemi, H. Kokkola, A. Nenes, Comprehensively accounting for the effect of giant CCN in cloud activation parameterizations. *Atmos. Chem. Phys.* **10**, 2467–2473 (2010). doi:10.5194/acp-10-2467-2010

70. C. E. Scott, A. Rap, D. V. Spracklen, P. M. Forster, K. S. Carslaw, G. W. Mann, K. J. Pringle, N. Kivekäs, M. Kulmala, H. Lihavainen, P. Tunved, The direct and indirect radiative effects of biogenic secondary organic aerosol. *Atmos. Chem. Phys.* **14**, 447–470 (2014). doi:10.5194/acp-14-447-2014

71. J. M. Edwards, A. Slingo, Studies with a flexible new radiation code, I: Choosing a configuration for a large-scale model. *Q. J. R. Meteorol. Soc.* **122**, 689–719 (1996). doi:10.1002/qj.49712253107